Novel Composite Thick-Film Electrodes Consisted of Zinc Oxide and Silicon for Lithium-Ion Battery Anode

Hiroyuki Usui, Takamasa Kono, and Hiroki Sakaguchi[*]

Department of Chemistry and Biotechnology, Graduate School of Engineering, Tottori University
4-101 Minami, Koyama-cho, Tottori 680-8552, Japan
[*]E-mail: sakaguch@chem.tottori-u.ac.jp

As a novel anode for Li-ion battery, ZnO/Si composite thick-film electrodes with various ratios of ZnO:Si were prepared by a gas-deposition method using a commercial Si powder and a radial-shaped ZnO powder synthesized by a precipitation method. We investigated the effect of the ZnO amount and the radial morphology on the anode performance, comparing with charge–discharge properties of a ZnO electrode without Si. The ZnO electrode showed a stable cyclability and a moderate discharge capacity of 160–220 mA h g^{-1} after the 20th cycle. The composite electrode of ZnO/Si with a ratio of 89/11 wt.% exhibited a good cycle stability after the 20th cycle and large discharge capacities exceeding the theoretical capacity of graphite until the 370th cycle. In contrast, a composite electrode containing of crushed ZnO showed a flat surface and poor performance. These results revealed that microstructure of the radial-shaped ZnO is very favorable for improving efficiencies of electrode reactions due to its high surface area, and is effective in accommodating the stresses induced by Li-insertion and Li-extraction in/from Si.
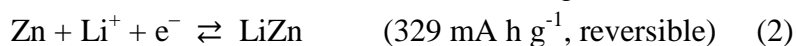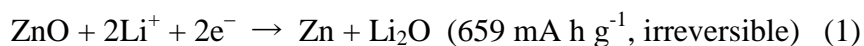
1. INTRODUCTION

Novel anode materials with a high energy density are required for next-generation Li-ion batteries in electric vehicles. In these days, Si-based materials have attracted much attention as a promising candidate of the anodes due to their high-specific capacity in comparison with the practical graphite anodes. Silicon has a very large specific capacity of 4200 mA h g^{-1}, which is more than ten times larger than that of 372 mA h g^{-1} in graphite anode. This huge capacity is originated from an alloying reaction of Li–Si in the composition range from Si to Li$_{4.4}$Si (Li$_{22}$Si$_5$) [1–3]. As other

advantages, Si is abundant, less expensive, and nontoxic. Thus, Si-based materials are very appropriate as next-generation anodes. It is, however, difficult to apply Si for practical anodes because Si has some critical disadvantages: a low intrinsic electrical conductivity, a low diffusion coefficient of Li in Si (10^{-14}–10^{-12} cm^2 s^{-1} [4–6]), and a drastic change of specific volume during the alloying/dealloying reactions. The volumetric change ratio per Si atom corresponds to be 410% [7–9], which is very serious as anode active material because the volumetric change causes a severe pulverization, an electrical isolation in the Si electrode, and a serious capacity fading. Considerable attempts have been carried out to overcome these problems. The attempts can be mainly classified in three ways. One is an alloying of Si and inactive elements such as transition metals to form silicides. When a silicide is used instead of elemental Si as the active material of the anode, the discharge capacity is drastically reduced because of the smaller storage amount of Li ions in the silicide. We believe that next-generation anode materials should mainly consist of elemental Si to derive the advantage of its huge theoretical capacity. The second way is structural modifications by utilizing amorphous Si [10] and nanostructured Si [11]. The third way is to synthesize a composite of Si as active material for Li and a less-active material such as carbon [12,13].

Gas-deposition (GD) method is very favorable for forming thick-film anodes and for improving their electrode performance, which has been recently demonstrated by the authors [14–21]. In this method, an aerosol consisting of raw particles and a carrier gas is jetted near the speed of sound from a nozzle onto a substrate. We have fabricated composite thick-film electrodes consisted of elemental Si particles and other materials such as metals and alloys. In these composite electrodes, the electrode performance was remarkably improved by synergetic effects based on the properties of Si and the combined metals [17–19] and alloys [15,16,21]. However, the effect of metal oxides on the electrochemical properties of composite GD-film electrodes has never been explored yet though the metal oxides are also attractive anode materials on account of their large theoretical capacities.

Zinc oxide (ZnO) has been investigated as an active material for Li-ion battery anodes [22–27] because ZnO is also abundant, less expensive, and nonhazardous. It exhibits Li-storage/extraction reactions with a total theoretical capacity of 988 mA h g^{-1} as following electrode reactions:

$$ZnO + 2Li^+ + 2e^- \rightarrow Zn + Li_2O \quad (659 \text{ mA h g}^{-1}, \text{ irreversible}) \quad (1)$$
$$Zn + Li^+ + e^- \rightleftarrows LiZn \quad (329 \text{ mA h g}^{-1}, \text{ reversible}) \quad (2)$$

Molar volumes of bulk ZnO, Zn, and Li$_2$O are 14.5, 18.2, and 14.8 cm^3 mol^{-1}, respectively. This indicates that a volumetric change from ZnO to Zn and Li$_2$O during Li insertion corresponds to 228% in the equation (1). The significant volume expansion brings on pulverization and an electrical isolation in the active material, resulting in a capacity fading and poor cycling performance. Furthermore, its low electronic conductivity and a slow kinetics of Li-ion diffusion in Zn [28–30] and ZnO [30] are also responsible for the poor performance. A size reduction of ZnO has been tried to improve the performance. As for nano-sized ZnO electrodes [25,26], however, the performance has not been drastically improved despite considerable efforts. In order to overcome the problem, the authors are herewith proposing GD-film electrodes consisted of microstructured ZnO prepared by a precipitation method, a new one-step approach for chemical synthesis of ZnO. This method has been

recently developed as a large-scale synthesis technique by some research groups, Yamabi *et al.* [31], Vayssieres *et al.* [32], and Li *et al.* [33]. The approach yields crystalline ZnO with a one-dimensional morphology in a strongly-basic aqueous solution containing $Zn(OH)_4^{2-}$ under mild conditions, atmospheric pressure and moderate temperatures below 90°C [31–35]. Following these studies, some researchers investigated a morphological control of ZnO, which revealed that ZnO microstructure can be easily controlled by varying growth conditions and by adding surfactants into the solutions [36–43].

In this study, we synthesized a radial-shaped ZnO powder as a microstructured anode material by the precipitation method. We prepared thick-film electrodes consisted of the radial-shaped ZnO by using the GD method, and investigated their electrochemical Li-insertion/extraction properties. To improve the performance of Si-based anode, ZnO/Si composite thick-film electrodes were prepared by using mixed source materials of ZnO and Si. We evaluated the performance of the composite electrodes and investigated the influence of the ZnO microstructure on their cycling performance.

2. EXPERIMENTAL

Zinc oxide powders were synthesized by a precipitation method using strongly-basic aqueous solutions. The synthetic conditions in this study were determined by reference to other reports [31–33], but some procedures have been developed by the authors [41–43]: an aqueous solution of 0.31 mol/L zinc sulfate heptahydrate ($ZnSO_4 \cdot 7H_2O$) with the volume of 32.5 mL was firstly prepared for Zn^{2+} ion source. We made 4.0 mol/L sodium hydroxide (NaOH) solution with 15 mL for pH adjustment, and 0.2 mol/L sodium dodecyl sulfate (SDS, $C_{12}H_{25}SO_4Na$) solution with 2.5 mL. The solutions of $ZnSO_4 \cdot 7H_2O$ and SDS were poured into a flask, and agitated by a magnetic stirrer with a speed of 1000 rpm. The NaOH solution was added to the mixed solution. The pH value of the mixed solution was around 13. The mixed solution was stirred for 60 minutes at 5°C to obtain transparent solutions containing $Zn(OH)_4^{2-}$ ions [31–33], and that was subsequently stirred for 90 minutes at room temperature for nucleation of crystalline ZnO [31–33,43]. Then, hot stirring of the mixed solution was performed for 5 hours at 85°C to produce a white-colored precipitation. During the hot stirring, ZnO crystal growth gradually promoted by dehydration between OH⁻ on the surface of the growing crystals and the OH⁻ ligands of the hydroxyl complexes [31]. In the presence of SDS surfactant, the ZnO crystal surface was chemically activated by surfactant micelles, thereby forming a morphology of radial-shaped ZnO [41,43]. To remove surfactant molecules, the precipitation was centrifuged and washed with deionized water for three times. The washed precipitation was dried in vacuum for 48 hours to obtain crystalline ZnO powder as a final product. All reagents were analytical grade and were used without further purification in the experiment. The crystal structure of ZnO was investigated by using an X-ray diffractometer (Ultima IV Rigaku Co., Ltd.) with CuKα radiation. Raman spectra of the powder were measured by using a Raman microscopy system (NanofinderFLEX, Tokyo Instruments, Inc.) at room temperature. As a reference sample, a commercial ZnO powder (purity 99.9%, Wako Pure Chemical Industries, Ltd.) was also measured.

For gas-deposition, copper foil substrates with 20 μm in thickness were set up in a vacuum chamber equipped a guide tube with a nozzle of 0.8 mm diameter [14–21]. The distance from the

nozzle to the substrate was set to be 10 mm. An aerosol consisting of Ar gas (differential pressure: 7×10^5 Pa) and active material powders was generated in the guide tube, and instantly gushed from the nozzle onto the Cu substrate in the chamber with a base pressure of 10 Pa. As active material powders, we set the precipitated ZnO powder to prepare ZnO thick-films, or a mixture of the ZnO and a commercial Si powder (purity 99.9%, Wako Pure Chemical Industries, Ltd.) to obtain ZnO/Si composite thick-films. To change the ratio of ZnO to Si in the obtained films, a blend ratio of ZnO:Si in the mixtures was varied. The weight ratios of ZnO/Si were 70/30, 75/25, and 89/11 wt.% in the thick-film electrodes, which was analyzed by means of an energy dispersive X-ray fluorescence (XRF) spectrometer (EDX-720 Shimadzu Co. Ltd.). The amount of the deposited active materials on the substrates was about 0.1 mg. The surface morphologies of the thick-films were observed using a field-emission scanning electron microscope (JSM-6701F JEOL Co., Ltd.).

Electrochemical measurements were carried out with a beaker-type three-electrode cell. The working electrodes were the obtained thick-film electrodes. Both counter and reference electrodes were 1-mm-thick Li metal sheets (Rare Metallic Co., Ltd., 99.90%). We used $LiClO_4$-dissolved in propylene carbonate (PC; $C_4H_6O_3$, Kishida Chemical Co., Ltd.) at a concentration of 1.0 M as the electrolyte. Constant current charge–discharge tests were performed using an electrochemical measurement system (HZ-3000 Hokuto Denko Co., Ltd.) under constant currents at 303 K with the cutoff potentials set as 0.005 V vs. Li/Li^+ for charge and 3.000 V vs. Li/Li^+ for discharge. The current densities were set to be 1.0 A g^{-1} (1.0C, 1C was defined as a current rate of three Li^+ reaction per hour; 988 mA g^{-1}) for ZnO electrodes, and 2.7–3.2 A g^{-1} (approximately 1.0C) for ZnO/Si composite electrodes. Cyclic voltammetry measurements were carried out using an electrochemical measurement system (Compactstat Ivium Technologies Co., Ltd.) at a scan rate of 0.1 mV s^{-1}.

3. RESULTS AND DISCUSSION

3.1 Electrochemical characterization of ZnO electrode

Figure 1(a) shows a FE-SEM image of the obtained powder by the precipitation method in this study. We observed hexagonal columns with a diameter of 50–500 nm and a length of 1–5 μm. These columns were densely aggregated, which typically formed a radial-shaped structure. The origin of the radial shape is chemically-activated surface of ZnO species by micelles of dodecyl sulfate ions [41,43]. Well-faceted prism planes were recognizable for the hexagonal columns. An inset in the figure is an enlarged view for a basal plane of a column. A regular hexagon can be seen on the basal plane, indicating the crystallization in the hexagonal system. Figure 1(b) depicts an XRD pattern of the precipitated powder. All diffraction peaks are very sharp and can be indexed as wurtzite ZnO (ICSD No. 00-36-1451). A crystalline size was estimated to be about 72 nm by using Scherrer formula. No diffraction peak of SDS surfactant and other materials was observed. These results revealed that the obtained powder consisted of ZnO with the radial-shaped morphology.
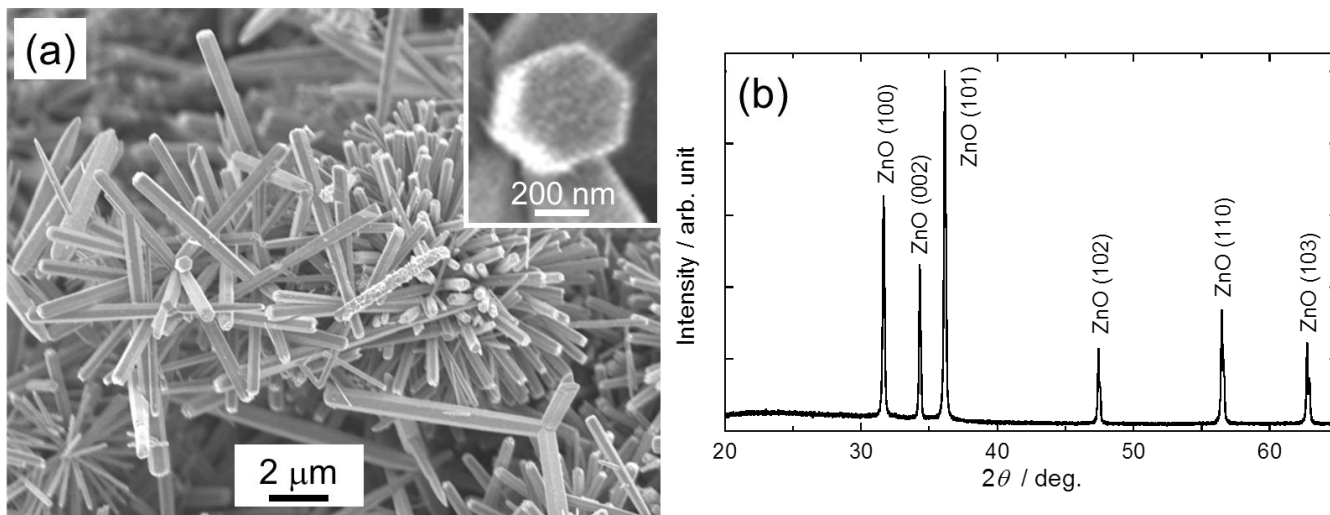
Figure 1. (a) FE-SEM image and (b) XRD pattern of precipitated powder for source material of gas-deposition process.
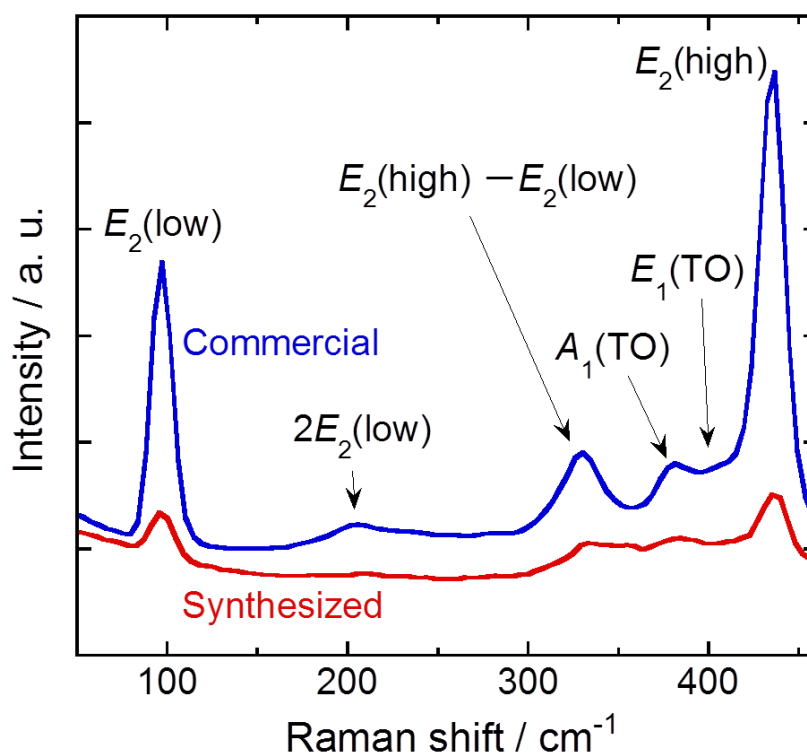

Figure 2. Raman spectra of commercial ZnO powder and synthesized ZnO powder by precipitation method.

Raman spectra of ZnO have been investigated by many researchers [44-48]. According to their studies, a single-crystalline ZnO has eight sets of optical phonon modes at Γ point of the Brillouin zone, classified as $A_1 + E_1 + 2E_2$ modes (Raman active), $2B_1$ modes (Raman inactive), and $A_1 + E_1$

modes (infrared active) [47]. The polar A_1 and E_1 modes split into longitudinal optical (LO) and transverse optical (TO) components with different wavenumbers due to the macroscopic electric fields associated with the LO phonons [48]. Nonpolar phonon modes with symmetry E_2 have two frequencies, E_2(high) is associated with oxygen atoms and E_2(low) is associated with oxygen displacement and sub-lattice. Figure 2 depicts Raman spectra of the commercial ZnO powder and the obtained ZnO powder by the precipitation method. Vibration peaks for the commercial ZnO can be clearly seen at 97, 206, 330, 381, 407, 436, and 583 cm^{-1}. The intense peaks at 97 and 436 cm^{-1} can be assigned as E_2(low) and E_2(high), respectively. The second-order peaks at 206 and 330 cm^{-1} were assigned as $2E_2$(low) and E_2(high)$-E_2$(low), respectively. The weak peaks located at 381 and 407 cm^{-1} are known to be the vibration modes of A_1(TO) and E_1(TO), respectively. On the other hand, the precipitated ZnO powder exhibited six peaks at the same positions as those of the commercial one though the peak intensities were relatively low. The characteristics of Raman spectra are in good agreement with the XRD results.
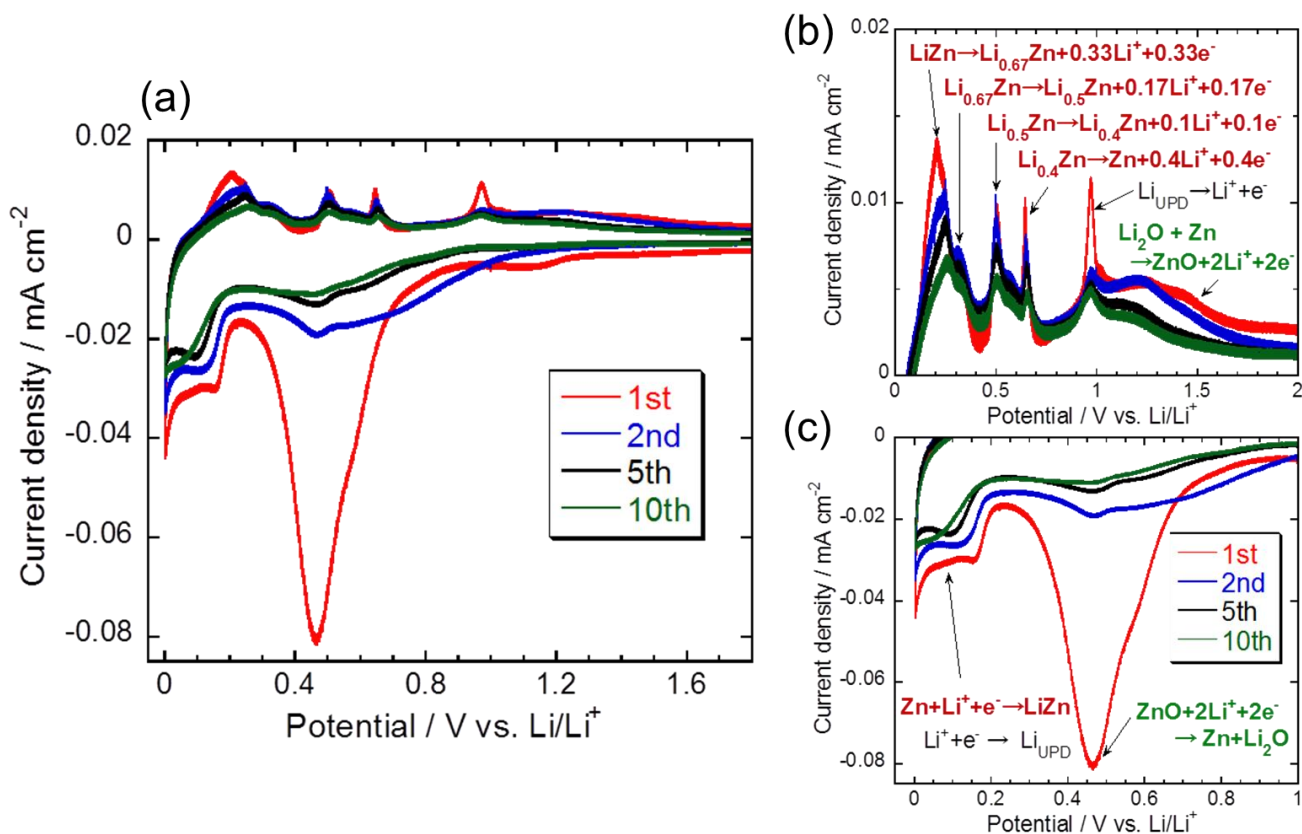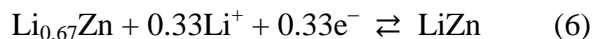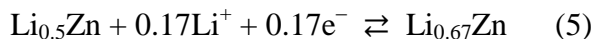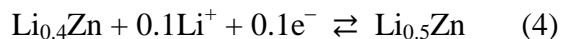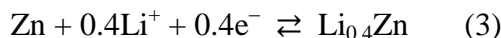

Figure 3. (a) Cyclic voltammograms of ZnO thick-film electrode prepared by gas-deposition method. Enlarged views of (b) anodic and (c) cathodic profiles

Figure 3 shows cyclic voltammograms of a ZnO thick-film electrode prepared by the gas-deposition method using a source powder of the precipitated ZnO. The chemical diffusion coefficient of Li ion in ZnO is very low ($10^{-14}-10^{-12}$ cm^2 s^{-1} [30]): Li diffusion in ZnO is very slow. To identify peak, sweep rate was set to be a low value, 0.1 mV s^{-1}. At the first cycle, a large cathodic peak appeared at 0.47 V vs. Li/Li$^+$ (Fig. 3(c)), which is attributed to a reducing ZnO to form Li$_2$O according

to the equation (1). At the following cycles, the peaks continued to appear though current densities of the peaks were significantly reduced. It is suggested that the reduction reaction partially occurs at the following cycles. Below the potential of 0.20 V vs. Li/Li$^+$, broad cathodic peaks appeared at every cycle. These peaks are ascribed to four-stage alloying/dealloying reactions of Li–Zn system as follows:

$$Zn + 0.4Li^+ + 0.4e^- \rightleftarrows Li_{0.4}Zn \qquad (3)$$
$$Li_{0.4}Zn + 0.1Li^+ + 0.1e^- \rightleftarrows Li_{0.5}Zn \qquad (4)$$
$$Li_{0.5}Zn + 0.17Li^+ + 0.17e^- \rightleftarrows Li_{0.67}Zn \qquad (5)$$
$$Li_{0.67}Zn + 0.33Li^+ + 0.33e^- \rightleftarrows LiZn \qquad (6)$$

We consider that four kinds of original cathodic peaks were merged into one peak due to the very slow kinetics of the first lithiation stage from Zn to Li$_{0.4}$Zn [28–30], which has been confirmed by Fujieda *et al.* [29]. In the first cycle of the delithiation process, four anodic peaks were observed at 0.20, 0.31, 0.52, and 0.66 V vs. Li/Li$^+$ (Fig. 3(b)), corresponding to the four-stage dealloying reactions of Li–Zn system described as the equations (3)–(6). The potentials of the four peaks were in good agreement with those in the previous reports [27,29,30]. Another peak located at 0.98 V vs. Li/Li$^+$ was presumably caused from a stripping of Li-underpotential deposition (Li-UPD) on Cu substrate [49–51]. In addition, a very-broad anodic peak can be observed in the potential range from 0.8 to 1.6 V vs. Li/Li$^+$, which is probably attributed to a reverse reaction of the equation (1), reduction of Li$_2$O and oxidation of Zn. This is one of the conversion reactions of metal oxides discovered by Tarascon *et al.* [52–55] and other groups [56–59]. In the subsequent cycles, the voltammogram profiles showed a good reproducibility. We can therefore suggest that the alloying/dealloying reactions of Li–Zn were reversible and that the conversion reaction of ZnO is partially reversible.

Figure 4(a) shows charge–discharge curves at the initial two cycles of the ZnO thick-film electrode. During the initial charge (lithiation) process, the electrode potential rapidly dropped to reach a plateau at 0.4–0.5 V vs. Li/Li$^+$, and then continuously decreased to 0.2 V. The potential plateau corresponds to the formation of Zn and Li$_2$O in the equation (1). Another plateau in the potential range of 0–0.2 V vs. Li/Li$^+$ indicates the alloying reactions of Li–Zn as mentioned in the interpretation for the voltammograms. During the first discharge (delithiation) process, some gentle shoulders were recognized from 0 to 1.5 V vs. Li/Li$^+$. According to the CV results, the dealloying of Li–Zn and the oxidation of Zn to ZnO are possibly responsible for the potential shoulders. At the first cycle, the charge and discharge capacities were 1140 and 340 mA h g^{-1}, resulting in a low coulombic efficiency of only 29%. The reason for the large irreversible capacity is that the formed Li$_2$O is not easily decomposed to elemental Li in the discharge process owing to a high thermodynamic stability of Li$_2$O (standard enthalpy of formation: –599 kJ mol^{-1}) [60]. On the following cycles, similar charge–discharge curves were obtained though the plateau of the charge process at 0.4–0.5 V shortened and inclined. From these results, the ZnO GD-film electrode also exhibited a characteristic electrochemical signature of the conversion reaction involved in transition-metal oxides [52].
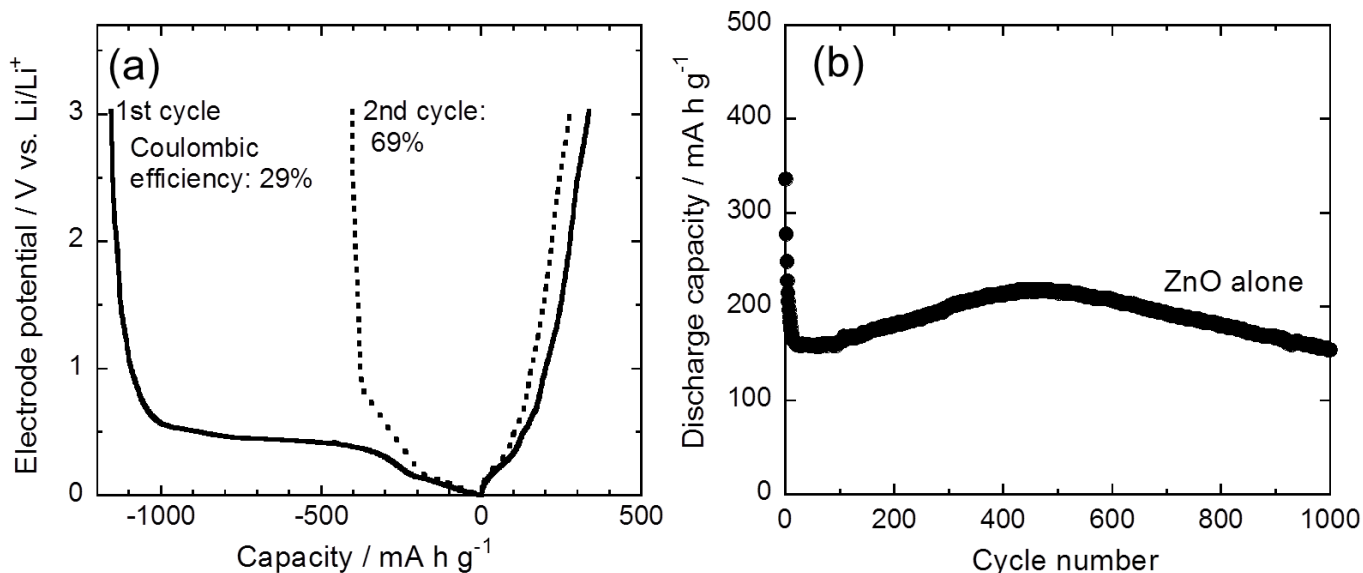
Figure 4. (a) Charge–discharge curves at the first and second cycles and (b) cycling performance of ZnO thick-film electrode.

Figure 4(b) gives dependence of the discharge capacity on the charge–discharge cycle for the ZnO electrode. The capacity rapidly reduced from 340 to 160 mA h g^{-1} within the initial 20 cycles, which is related to the formation of inactive Li$_2$O. In the subsequent cycles, the electrode exhibited very stable cycling performance and a moderate discharge capacity of 160–220 mA h g^{-1} though the capacity was lower than the theoretical capacity of graphite. In view of the stable cycling performance, the ZnO obtained by the precipitation method would be a feasible material to be combined with Si in our composite GD-film electrodes. In addition to the stable performance with the moderate capacity, the ZnO electrode is expected to have a high surface area because the radial-shaped ZnO powder with the unique morphology formed the thick film. In general, such high surface area is of great advantage to improve performance not only in Li-ion battery but also in other electrochemical devices, super capacitors [61], dye-sensitized solar cells [62], and photocatalysts [63].

3.2 Anode performance of ZnO/Si composite electrodes

Figure 5 shows charge–discharge curves at the initial two cycles for ZnO/Si composite thick-film electrodes with different weight ratios of ZnO to Si. The three electrodes behaved very alike. At the first cycle, these composite electrodes also showed potential plateaus at 0.4–0.5 V originated from the reducing of ZnO as is the case with the ZnO electrode. In addition to these, we clearly observed plateaus in charge and discharge processes at 0.05 V and 0.46 V vs. Li/Li$^+$, respectively. These potential plateaus are attributed to the alloying/dealloying reactions of Li–Si. We have proposed that an active material, combined with Si in composite electrodes, should be prohibited from blocking out Li-ion storage in the active material to enable efficient Li-ion transportation into/from Si [15,16,21]. The ZnO has a moderate Li-storage ability; moderate discharge capacities of 160–220 mA h g^{-1} were achieved after the initial capacity decay as demonstrated in Fig. 4.
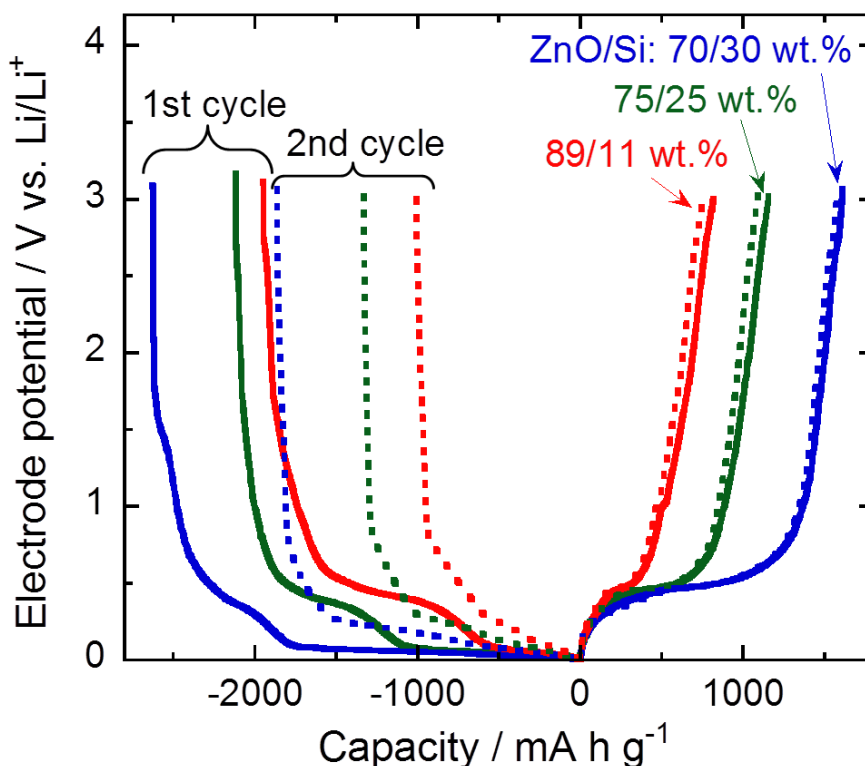
Figure 5. Charge–discharge curves at the initial two cycles of ZnO/Si composite thick-film electrodes with different weight ratios of ZnO and Si.

We consider that Li-insertion and Li-extraction into/from Si were promoted in the ZnO/Si composite electrodes because of the moderate Li-storage ability of ZnO. The inclined plateaus in charge process at the second cycle are possibly related to amorphization of Si by the first Li-insertion/extraction. With decreasing the weight ratio of Si in the composite electrodes, the charge and discharge capacities were reduced. We thus found that the Si amount involved in the electrodes basically contributes to their charge and discharge capacities because of much larger theoretical capacity of Si than that of ZnO.

Figure 6 summarizes cycling performance of these composite electrodes. For comparison, the data were also plotted in the figure for two electrodes of Si alone and ZnO alone. A large discharge capacity of approximately 2000 mA h g^{-1} has been confirmed for the Si electrode. A very steep decay of the discharge capacity was, however, observed by the 100th cycle. The capacity decay is attributed to pulverization and an electrical isolation of the active materials induced by drastic changes of silicon's volume during Li-insertion/extraction. A similar capacity decay was observed in case of the ZnO/Si composite electrode including 30 wt.% of Si. It is suggested that the relatively-large amount of Si brought on the pulverization and the electrical isolation of the composite electrode. The ZnO/Si electrode with the ratio of 75/25 wt.% shows a smaller initial capacity of 1160 mA h g^{-1} and the capacity fading was slightly improved.
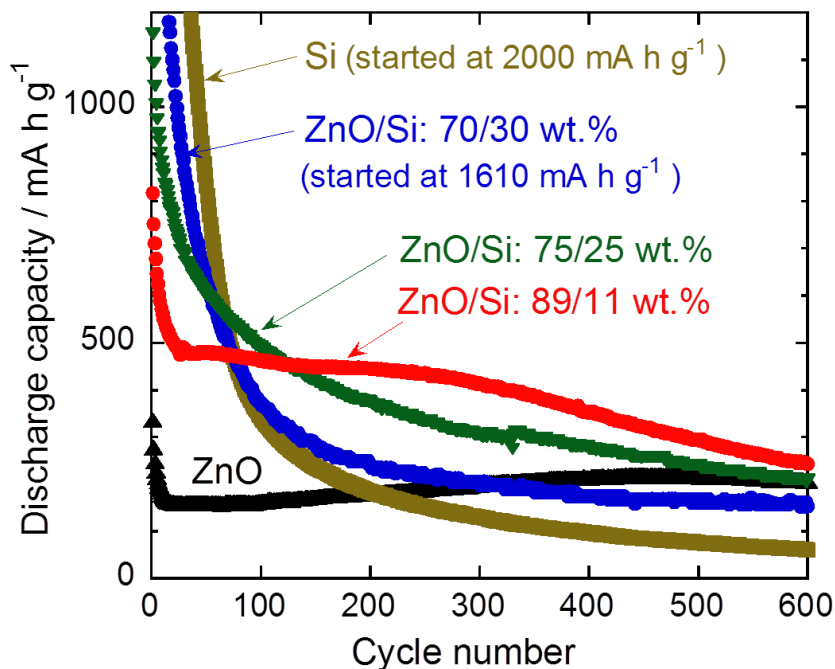
Figure 6. Dependence of discharge capacity on charge–discharge cycle for ZnO/Si composite thick-film electrodes.

On the other hand, the composite electrode containing 11 wt.% of Si exhibited a good cycle stability after the 20th cycle while a rapid capacity drop from 820 to 500 mA h g^{-1} was observed in the initial 20 cycles. This behavior closely resembles that of the ZnO electrode. It is a remarkable result that the capacity of the composite electrode have exceeded the theoretical capacity of graphite anode (372 mA h g^{-1}) until 370th cycle.

3.3 Effect of ZnO microstructure on electrode performance

To clarify the reason for the better cycling performance of the composite electrode, we investigated the influence of ZnO microstructure on the electrode performance. Figure 7 compares cycling performance of two kinds of ZnO/Si composite electrodes. One is the above-mentioned ZnO/Si electrode with 89/11 in wt.%. The other is a composite electrode prepared by GD using a source material consisted of Si and a crushed ZnO powder by a milling process in an agate mortar in order to break up the unique microstructure of hexagonal ZnO columns. Its weight ratio was 90/10 wt.%, which is nearly the same as that of the electrode using pristine ZnO. The composite electrode using the crushed ZnO exhibited low performance; a very small capacity of 300 mA h g^{-1} was obtained at the first cycle and the capacity was continuously decreased. Obviously, on the other hand, the composite electrode containing pristine ZnO have delivered much better electrode performance.
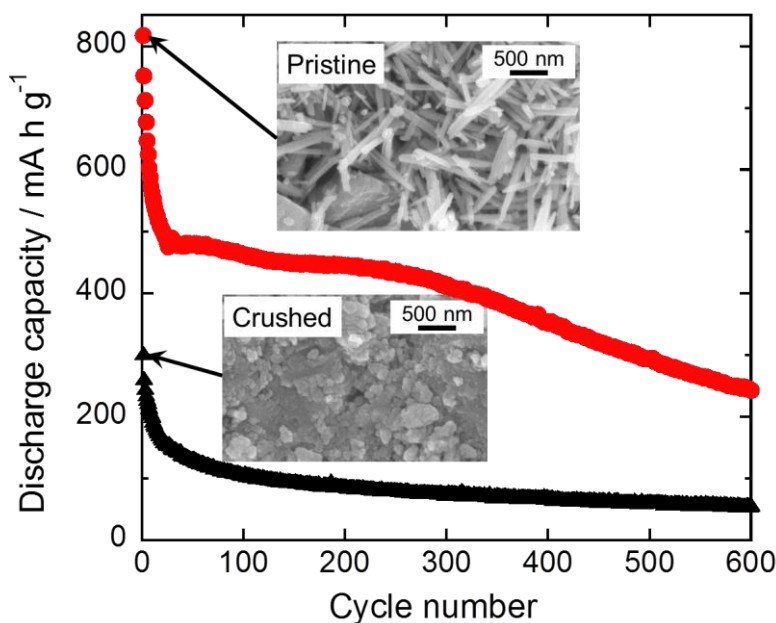
Figure 7. Influence of crushed ZnO on cycling performance of ZnO/Si composite thick-film electrodes.

Insets in Fig. 7 display FE-SEM images of these electrodes before the charge–discharge. In case of the electrode containing pristine ZnO, hexagonal ZnO columns were densely aggregated to form numerous interspaces on the surface. Such microstructure would be very favorable for improving efficiencies of electrode reactions due to its high surface area, and for enhancing charge/discharge capacities. In addition, the microstructure with the many interspaces can effectively accommodate the stresses induced by Li-insertion/extraction. The accommodation suppresses the pulverization of the active materials, and thus improves the cycle stability of electrode. By contrast, we observed a flatter surface morphology for the electrode consisted of crushed ZnO. No interspace was found on the surface unlike the other electrode because the radial shape and hexagonal columns of ZnO were broken up by the milling process before the deposition. Therefore, a lower surface area of the electrode limits the efficiency of electrode reactions to considerably reduce its discharge capacity. These results clearly revealed that the radial-shaped ZnO prepared by the precipitation method has the unique microstructure effective for improving the electrode performance of ZnO/Si composite electrodes because of the moderate Li-storage ability of ZnO and the numerous interspaces between the hexagonal ZnO columns.

4. CONCLUSION

The radial-shaped ZnO powder was synthesized by the precipitation method as the active material to be combined with Si in composite thick-film anode for next-generation Li-ion batteries. The ZnO/Si composite thick-film electrodes were prepared by the gas-deposition method using the obtained ZnO and Si. We evaluated the anode performance for the ZnO/Si composite electrodes, comparing with the electrochemical properties of the ZnO electrode without Si. Two kinds of electrode

reactions, the reversible alloying/dealloying reactions of Li–Zn and the partially-reversible conversion reaction of ZnO with Li, were confirmed by the CV measurements of the ZnO electrode. We observed that the ZnO electrode has the stable cycle stability and the moderate Li-storage ability. The composite electrode of ZnO/Si with 89/11 in wt.% exhibited the better cycle stability after the 20th cycle and the relatively-large discharge capacities exceeding the theoretical capacity of graphite until 370th cycle. In contrast, the composite electrode consisted of crushed ZnO showed the flatter surface morphology and the lower electrode performance in comparison with that using radial-shaped ZnO. These results revealed that the radial-shaped ZnO has a very favorable microstructure for improving efficiencies of electrode reactions due to its high surface area, and that the microstructure is effective in accommodating the stresses induced by Li-insertion and Li-extraction in/from Si.

References

1. J. O. Besenhard. J. Yang, M. Winter, *J. Power Sources*, 68 (1997) 87.
2. U. Kasavajjula, C. S. Wang, A. J. Appleby, *J. Power Sources*, 163 (2007) 1003.
3. N. Ding, J. Xu, Y. Yao, G. Wegner, I. Lieberwirth, C. Chena, *J. Power Sources*, 192 (2009) 644.
4. H. Xia, S. Tang, L. Lu, *Mater. Res. Bull.*, 42 (2007) 1301.
5. N. Ding, J. Xu, Y. X. Yao, G. Wegner, X. Fang, C. H. Chen, I. Lieberwirth, *Solid State Ionics*, 180 (2009) 222.
6. J. Xie, N. Imanishi, T. Zhang, A. Hirano, Y. Takeda, O. Yamamoto, *Mater. Chem. Phys.*, 120 (2010) 421.
7. C. J. Wen, R. A. Huggins, *J. Solid State Chem.*, 37 (1981) 271.
8. V. L. Chevrier, J. W. Zwanziger, J. R. Dahn, *J. Alloys Compd.*, 496 (2010) 25.
9. H. Kim, C.-Y. Chou, J. G. Ekerdt, G. S. Hwang, *J. Phys. Chem. C*, 115 (2011) 2515.
10. K.-L. Lee, J.-Y. Jung, S.-W. Lee, H.-S. Moon, J.-W. Park, *J. Power Sources*, 129 (2004) 270.
11. M.-H. Park, M. G. Kim, J. Joo, K. Kim, J. Kim, S. Ahn, Y. Cui, J. Cho, *Nano Lett.*, 9 (2009) 3844.
12. I.-S. Kim, P. N. Kumta, J. Power Sources, 136 (2004) 145.
13. Y. Zhang, X. G. Zhang, H. L. Zhang, Z. G. Zhao, F. Li, C. Liu, H. M. Cheng, *Electrochim. Acta*, 51 (2006) 4994.
14. H. Sakaguchi, T. Toda, Y. Nagao, T. Esaka, *Electrochem. Solid-State Lett.*, 10 (2007) J146.
15. T. Iida, T. Hirono, N. Shibamura, H. Sakaguchi, *Electrochemistry*, 76 (2008) 644.
16. H. Sakaguchi, T. Iida, M. Itoh, N. Shibamura, T. Hirono, *IOP Conf. Series: Mater. Sci. Eng.*, 1 (2009) 012030-1.
17. H. Usui, Y. Kashiwa, T. Iida, H. Sakaguchi, *J. Power Sources*, 195 (2010) 3649.
18. H. Usui, H. Nishinami, T. Iida, H. Sakaguchi, *Electrochemistry*, 78 (2010) 329.
19. H. Usui, M. Shibata, K. Nakai, H. Sakaguchi, *J. Power Sources*, 196 (2011) 2143.
20. H. Usui, Y. Yamamoto, K. Yoshiyama, T. Itoh, H. Sakaguchi, *J. Power Sources*, 196 (2011) 3911.
21. H. Usui, K. Meabara, K. Nakai, H. Sakaguchi, *Int. J. Electrochem. Sci.*, 6 (2011) 2246.
22. F. Belliard, P. A. Connor, J. T. S. Irvine, *Ionics*, 5 (1999) 450.
23. F. Belliard, P. A. Connor, J. T. S. Irvine, *Solid State Ionics*, 135 (2000) 163.

24. F. Belliard, J. T. S. Irvine, *J. Power Sources*, 97-98 (2001) 219.
25. J. P. Liu, Y. Y. Li, X. T. Huang, G. Y. Li, Z. K. Li, *Adv. Funct. Mater.*, 18 (2008) 1448.
26. J. Liu, Y. Li, R. Ding, J. Jiang, Y. Hu, X. Ji, Q. Chi, Z. Zhu, X. Huang, *J. Phys. Chem. C*, 113 (2009) 5336.
27. H. Wang, Q. Pana, Y. Cheng, J. Zhao, G. Yin, *Electrochim. Acta*, 54 (2009) 2851.
28. J. Wang, P. King, R. A. Huggins, *Solid State Ionics*, 20 (1986) 185.
29. T. Fujieda, S. Takahashi, S. Higuchi, *J. Power Sources*, 40 (1992) 283.
30. J. Xie, N. Imanishi, A. Hirano, Y. Takeda, O. Yamamoto, X. B. Zhao, G. S. Cao, *Thin Solid Films*, 519 (2011) 3373.
31. S. Yamabi, H. Imai, *J. Mater. Chem.*, 12 (2002) 3773.
32. L. Vayssieres, *Adv. Mater.*, 15 (2003) 464.
33. P. Li, Y. Wei, H. Liu, X.K. Wang, *Chem. Commun.*, 24 (2004) 2856.
34. W. W. He, Y. P. Li, Z. Q. Chen, Y. Q. Wang, R.Y . Zhang, *Mater. Lett.*, 60 (2006) 2299.
35. J. Liu, X. Huang, Y. Li, J. Duan, H. Ai, *Mater. Chem. Phys.*, 98 (2006) 523.
36. Y. Masuda, N. Kinoshita, K. Koumoto, *Electrochim. Acta*, 53 (2007) 171.
37. P. Li, H. Liu, Y.F. Zhang, Y. Wei, X.K. Wang, *Mater. Chem. Phys.*, 106 (2007) 63.
38. S. T. He, H. Maeda, M. Uehara, M. Miyazaki, *Mater. Lett.*, 61 (2007) 626.
39. L. Tang, B. Zhou, Y. Tian, H. Bala, Y. Pan, S. Ren, Y. Wang, X. Lv, M. Li, Z. Wang, *Colloid Surf. A*, 296 (2007) 92.
40. R. Wahab, S. G. Ansari, Y. S. Kim, H. K. Seo, G. S. Kim, G. Khang, H.-S. Shin, *Mater. Res. Bull.*, 42 (2007) 1640.
41. H. Usui, *J. Phys. Chem. C*, 111 (2007) 9060.
42. H. Usui, *Mater. Lett.*, 63 (2009) 1489.
43. H. Usui, *J. Colloid Interface Sci.*, 336 (2009) 667.
44. T. C. Damen, S. P. S. Porto, B. Tell, *Phys. Rev.*, 142 (1966) 570.
45. J. M. Calleja, M. Cardona, *Phys. Rev. B*, 16 (1977) 3753.
46. Y. J. Xing, Z. H. Xi, Z. Q. Xue, X. D. Zhang, J. H. Song, R. M. Wang, J. Xu, Y. Song, S. L. Zhang, D. P. Yu, *Appl. Phys. Lett.*, 83 (2003) 1689.
47. J. H. Zheng, Q. Jiang, J. S. Lian, *Appl. Surf. Sci.*, 258 (2011) 93.
48. S. Sahoo, G. L. Sharma, R. S. Katiyar, *J. Raman Spectrosc.*, 43 (2012) 72.
49. D. M. Kolb, M. Przasnyski, H Gerischer, *Electroanal. Chem. Interfacial Electrochem.*, 54 (1976) 25.
50. L.-F. Li, D. Totir, Y. Gofer, G. S. Chottiner, D. A. Scherson, *Electrochm. Acta*, 44 (1998) 949.
51. M. Moshkovich, Y. Gofer, D. Aurbach, *J. Electrochem. Soc.*, 148 (2001) E155.
52. P. Poizot, S. Laruelle, S. Grugeon, L. Dupont, J.-M. Tarascon, *Nature*, 407 (2000) 496.
53. S. Grugeon, S. Laruelle, R. H. Urbina, L. Dupont, P. Poizot, J.-M. Tarascon, *J. Electrochem. Soc.*, 149 (2001) A285.
54. P. Poizot, S. Laruelle, S. Grugeon, J.-M. Tarascon, *J. Electrochem. Soc.*, 149 (2002) A1212.
55. S. Mitra, P. Poizot, A. Finke, J.-M. Tarascon, *Adv. Funct. Mater.*, 16 (2006) 2281.
56. J. Cabana, L. Monconduit , D. Larcher , M. R. Palacín, *Adv. Mater.*, 22 (2010) E170.
57. P. Balaya, H. Li, L. Kienle, J. Maier, *Adv. Funct. Mater.*, 13 (2003) 621.
58. O. Delmer, P. Balaya, L. Kienle, J. Maier, *Adv. Mater.*, 20 (2008) 501.
59. E. Bekaert, P. Balaya, S. Murugavel, J. Maier, M. Ménétrier, *Chem. Mater.*, 21 (2009) 856.
60. G. K. Johnson, R. T. Grow, W. N. Hubbard, *J. Chem. Thermodynamics*, 7 (1975) 781.
61. M. Jayalakshmi, M. Palaniappa, K. Balasubramanian, *Int. J. Electrochem. Sci.*, 3 (2008) 96.
62. M. H. Lai, M. W. Lee, G.-J. Wang, M. F. Tai, *Int. J. Electrochem. Sci.*, 6 (2011) 2122.
63. J. A. R. Márquez, C. M. B. Rodríguez, C. M. Herrera, E. R. Rosas, O. Z. Angel, O. T. Pozos, *Int. J. Electrochem. Sci.*, 6 (2011) 4059.